SSIM 2023 – PM Dight (ed.)

doi:10.36487/ACG_repo/2335_49

Rockfalls as precursory strain indicators leading to a large slope failure ('Leo Failure') at Bingham Canyon Mine, USA

KW Schafer *Rio Tinto, USA*

KM Bakken *Rio Tinto, USA*

S Ergun *Rio Tinto, USA*

J Potter *Geotechnical Center of Excellence, The University of Arizona, USA*

BJ Ross *Geotechnical Center of Excellence, The University of Arizona, USA*

JA Telfer *Rio Tinto, USA*

CP Williams *Rio Tinto, USA*

Abstract

Rockfalls and rockslides are ubiquitous hazards at the Bingham Canyon Mine, where a large (19×10^6 tonnes) slope failure ('Leo Failure') occurred on 31 May 2021. The deforming slope was monitored with continuous thermal video recordings. This study documents (based upon thermal video review) both the frequency and spatial distribution of rockfalls leading to the slope failure. Thermal video monitoring began approximately four days prior to collapse, during the final acceleration phase. The frequency of rockfalls increases exponentially leading to failure, with approximately 45% of the total documented rockfalls (158) occurring within six hours of the failure. Of the documented rockfalls 88% are spatially coincident (within 15 m) with a left, the right, and crestal failure boundaries, but not the break-out at the toe.

The majority of rockfalls (60%) repeatedly originate from nearly the same positions within three different areas (clusters): Cluster 1 positioned along the right-release, a bedding-parallel fault with clay-gouge; and both clusters 2 and 3 positioned along a multi-staged left-release, a complex intra-intrusive, fractured igneous contact. Approximately twice the number of rockfalls originate from each of both Cluster 2 (N = 44) and Cluster 3 (N=33) as compared to Cluster 1 (N=19). The cumulative rockfall versus time curve for Cluster 1, along the contiguous faulted-bedding right-release, generally exhibits a progressive acceleration up to the time of failure. In contrast, a cumulative rockfall curve for Cluster 2, along a geometrically complex left-release, exhibits a series of three abrupt periods of rapid rockfall accelerations (e.g. 1–1.5 per day to 70–75 per day). The cyclical accelerations and greater number of rockfalls are attributed to brittle strain localisation at geometric asperities associated with an evolving 'step-path' left-release, as opposed to creep-strain along an inherited, clay-rich sedimentary contact reactivated as a fault.

Keywords: *rockfall, slope failure, slope stability in open pit mines*

1 Introduction

A 'rockfall' generally refers to downslope rolling, tumbling, and translating of cm to m-scale rocks. Rockfalls are a ubiquitous safety concern at active mine slopes where the presence of both personnel and equipment are at risk. Rockfalls are transient phenomena that can result from a wide range of conditions present in surface mining; e.g. blasting and scaling; degradation associated with surface weathering phenomena such as hydrolytic weakening, surface water runoff, or freeze-thaw spalling (Read & Stacey 2009). More importantly, rockfalls can be precursory events to larger-scale failures (Rosser et al. 2007; Kromer et al. 2015) that could pose a significant risk to both personnel and equipment; and potentially diminish the economic value of a mining operation.

The large-scale (tens of metres to 1,000 m) collapse/failure of an open pit slope may adhere to a three-phase cyclicity of time-dependent displacement (Broadbent & Zavodni 1983; Zavodoni 2001). This cycle is remarkably similar to time-dependent strain measured in laboratory, rock-deformation creep experiments (e.g. Hobbs 1976): An initial, transient acceleration of strain-rate (primary creep); followed by a regression (de-acceleration) in strain-rate leading to steady-state (secondary creep); followed, in-turn, by a final progressive strain acceleration ultimately leading to slope collapse (tertiary creep). In the case of slope failures, the constitutive behaviour of rocks is primarily pressure-dependent with strain accommodated by reactivation of a diverse population of structural discontinuities present over a range of scales or brittle fracture to create new structural discontinuities. However, the time-dependent displacement behaviour implies a time-dependent constitutive behaviour, or deformation mechanism to accommodate the strain of the deforming slope subjected to a constant gravitational load. This could include a sub-critical crack-growth mechanism occurring over a range of scales, such as micro-fracture propagation and coalescence to sub-critical propagation of existing discontinuities (e.g. Kemeny 1991; Shao et al. 1997).

Most case-studies of slope collapse use a measure of slope movement, such as displacement, to describe either a power or exponential trend to the progressive (tertiary creep) final phase of damage accumulation leading to megascopic brittle failure. A common practice is to invert the final, progressive-stage velocities and fit a straight line in velocity-1 (1/velocity) versus time-space where the horizontal axis (time) intercept is the time at which failure is expected to occur (e.g. Fukuzono 1985; Rose & Hungr 2006). Although a linear fit is both practical and mathematically convenient, slope acceleration trending towards collapse/failure is rarely, if ever, linear when measured over a sufficient time-period (Rose & Hungr 2006).

Voight (1988) suggests that a power-law describing the terminal stages of failure should be reflected in other measurable (precursory) deformation including strain, seismicity rate, and seismic energy release. Early studies of precursory events leading to catastrophic failure focused on predicting earthquakes and volcanic eruptions (Byerlee 1978; Voight 1988).

Acoustic energy release is a natural byproduct of intra- and inter-granular microcracking. Acoustic emissions rates measured in conventional triaxial rock-deformation experiments directly correlate to inelastic strain rates and are reliable indicators of approaching mechanical failure (Lockner & Byerlee 1992; Lockner 1993). In these experiments microcracks spatially concentrate late in the loading; near peak stress in a constant strain-rate experiment or at the onset of the tertiary creep phase in a constant-stress experiment (Lockner 1993).

Natural examples of precursory inelastic strain events (damage accumulation) leading to slope failures include a study of a chalk-cliff exposed along a shore in Western France where a power-law acceleration of both seismic rate and energy preceded a slope collapse (Armitrano et al. 2005; Senfaute et al. 2009); and the study of a cliff exposed on the east coast of the UK where rockfall frequency and magnitude (volume) increased towards the time of slope failures (Rosser et al. 2007). Rosser et al. (2007) also posits that both the rate and volume of precursory rockfall material could be proportional to the magnitude of the final failure volume. Kromer et al. (2015), documented both an increase in frequency of rockfalls leading to slope failure and a spatial coincidence of rockfall locations with the perimeter of the deforming rock mass.

The primary data used in this study are continuous recordings (24 hours per day, 15 frames per second) of thermal, infrared video of the monitored slope beginning approximately five days prior to the Leo Failure. Thermal infrared cameras detect radiated heat energy and require no visible light (i.e. provide video imagery in both day and night conditions) and can provide a viable remote monitoring solution for both geotechnical hazards and situational awareness in surface mining environments (Wellman et al. 2022). The selected thermal video camera (Teledyne FLIR ID-632 640 × 480 pixel, security camera) provides a 32-degree (horizontal) and a 26-degree (vertical) field-of-view (Figure 1). The entire pre-failure slope is within the thermal camera field-of-view except for a portion (lower-left) of the two lowermost benches, each with a 15.2 m (50 ft) height.

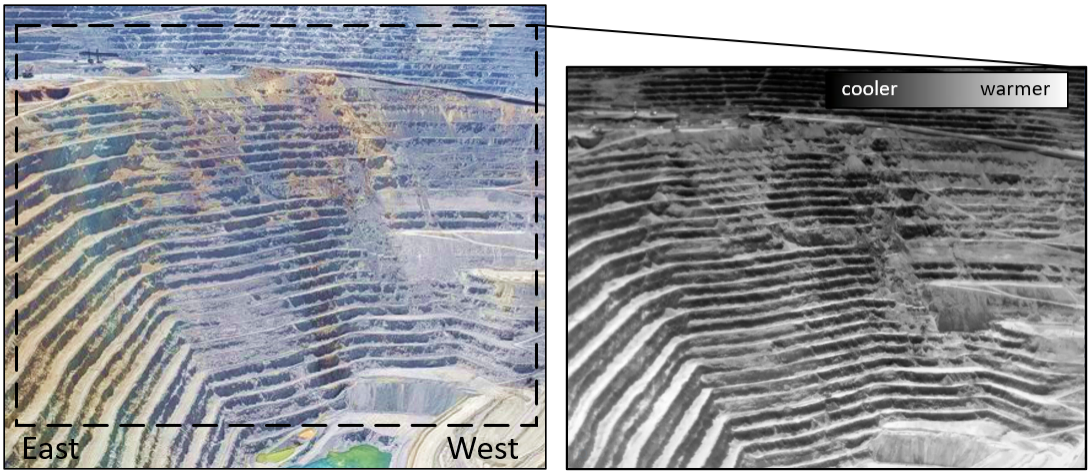

(a) (b)

Figure 1 Photograph (a) and thermal image (b) of the monitored pit slope prior to the Leo slope failure

For several days leading to the Leo Failure, real-time interpretation of the thermal video data indicated an increase in frequency of rockfalls consistent with an increase in both displacement and acceleration observed in slope-monitoring radar data. Real-time monitoring also indicated that rockfalls appear to initiate along the perimeter of the future slope-failure boundaries.

Similar to Rosser et al. (2007), this research documents an exponential or power increase in the total number of rockfalls leading to the occurrence of the Leo Failure occurring during morning day-light conditions on May 31, 2021. We then relate the spatial distribution and frequency variation of rockfalls to both critical structural discontinuities governing the ultimate failure and proposed deformation mechanisms.

2 Description of the pre-failure, pit slope

The monitored pit slope is within the Bingham Canyon copper mine in Utah, USA. Thermal camera monitoring was initiated on 26 May 2021 and continued to August 3, 2021. The pit slope was selected for monitoring following a review of the mine-site, slope-monitoring sensors that indicated an acceleration of movement within the south wall of the pit. The thermal camera was positioned on the opposite side of the pit, at an elevation of 792 m (6,200 ft). The mine elevation ranges from 1,200 m (4,000 ft) to 2,130 m (7,000 ft) above sea level. Figure 1 illustrates the scene observed from the camera in a thermal infrared image using a grayscale colour palette where lighter shades are thermally warmer. The camera field-of-view is directed south to a north-facing pit slope. The single-bench elevation increment is approximately 15 m (50 ft). The north dipping inter-ramp angle of the slope prior to failure was between 37 and 38 degrees depending upon both slope azimuth and elevation. Approximately 400–450 m (1,300–1,500 ft) of vertical elevation is visible in the thermal camera field-of-view with the camera positioned approximately 2,100 m (7,000 ft) from the toe of the slope.

3 General description of the slope failure (Leo Failure)

The Leo Failure occurred within multiple lithologies, including: quartzite, limestone, monzonite, and porphyritic, quartz-monzonite; abbreviated as PQM. (Figure 2). The Leo Failure is bound to the west by the base of the Lark Bed, a sedimentary, lithologic contact tectonically reactivated as a fault. Local to the failure, the Lark bedding-parallel fault dips at approximately 40–50° in approximately the same direction of the slope. The Lark bedding-parallel fault-core varies in thickness from approximately 0.1 up to 0.9 m (3 in to 3 ft) and includes sheared clay-sized gouge and clay minerals. The Lark bedding-parallel fault and associated fault gouge is relatively weak based upon strengths estimated from laboratory shear-strength testing. Friction angles range from 18 to 22° and cohesion ranges from approximately 20 to 30 kPa.

The Leo Failure occurred on May 31, 2021, in three stages (or modes), initiating at the crest and generally propagating from the west to the east as the mass moved downslope (Figure 3). A first stage of failure ('Main Leo' block or segment) is bound to the west by the Lark Bed (right-release) and to the east by an intrusive igneous contact of PQM with monzonite (left-release). The secondary and tertiary blocks ('Left Leo') followed downslope and to the west (downward and clockwise translation), into the void left by the Main Leo slide-mass (Figure 3). The total failure weight is approximately 19 million tonnes. Rockfalls were clustered on the side releases of the Main Leo failure boundaries (discussed in the next section).

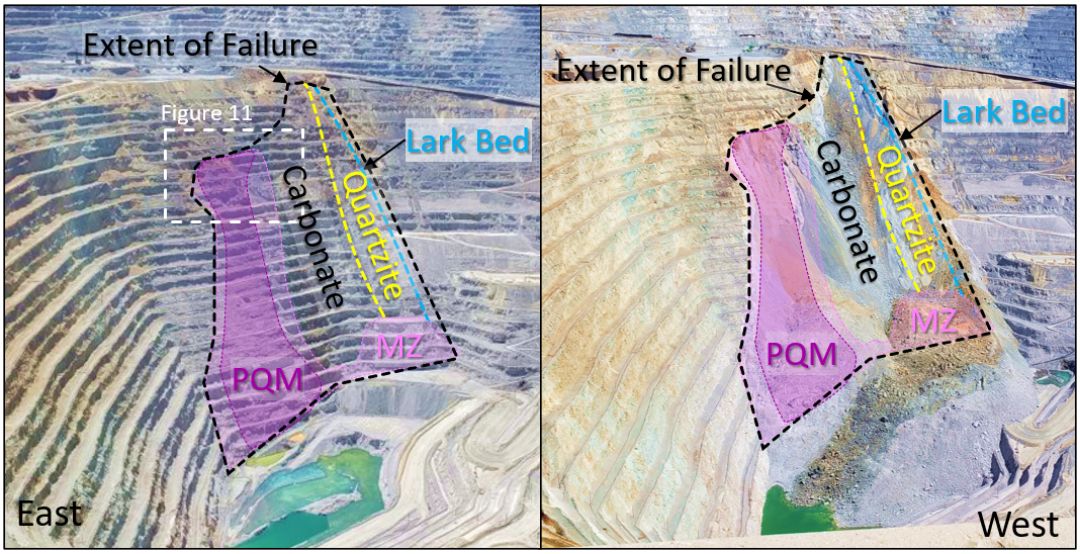

(a) (b)

Figure 2 (a) Photograph of the pit slope prior to the Leo Failure with generalised contacts for the lithologic units within the failure boundary; (b) Photograph of the post-failure slope with generalised key lithologic units within the failure boundary

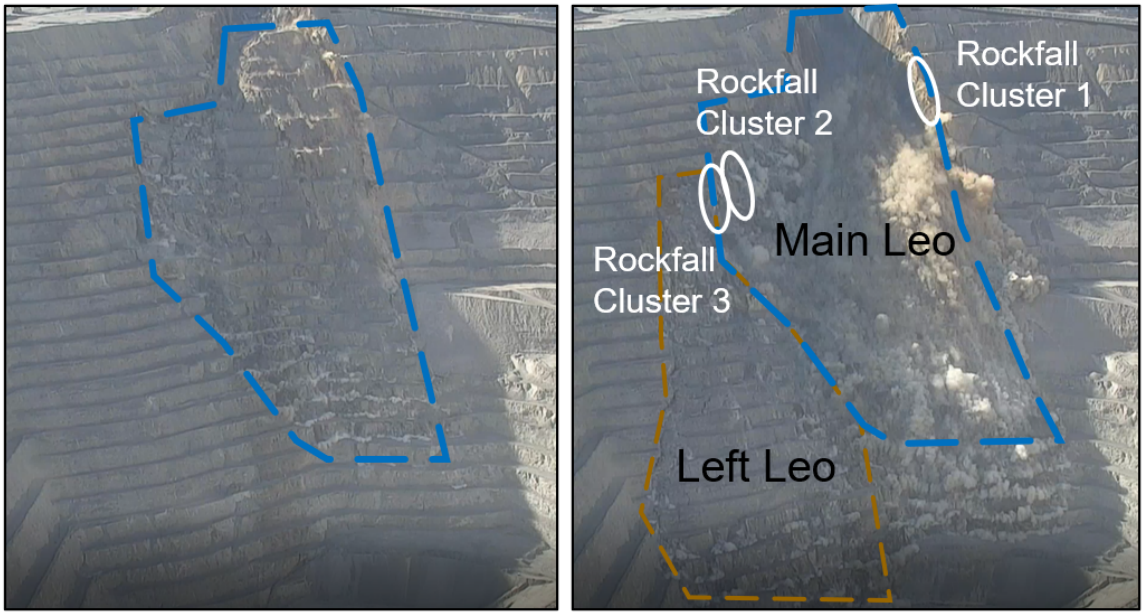

(a) (b)

Figure 3 Photographs of the early stages of the Leo Failure. (a) Outline of the primary failure stage, Main Leo; (b) Outline of the secondary to tertiary failure stages, Left Leo, and locations of rockfall clusters prior to the failure

4 Spatial and temporal analysis of rockfalls

Rockfalls can be discerned in thermal video images by the occurrence of thermal anomalies ('thermal scarring') associated with a ground disturbance that exposes either thermally cooler or thermally warmer rock with respect to the surrounding surficial temperature (Wellman et al. 2022). The thermal anomaly could be related to several conditions including: plowing loose rock down the slope, generation of fine-grained dust, or fragmentation of either the falling or impacted rock. The estimated size of the falling rock is based upon the pixel resolution (in this case approximately 0.4–0.5 m^2 or 4–5 ft^2). In this dataset, there are very few instances for which the size of the actual falling rock can be discerned with confidence. Of the 158 documented rockfalls only two could be discriminated from the associated thermal scarring (each approximately two pixels). A systematic analysis of how many rockfalls occur that are either not detected by the thermal camera or were overlooked in the video analysis is not available. However, a preliminary review of higher-resolution thermal-videos (imaging portions of the same slope) yielded results consistent with thermal camera video used in this analysis.

The estimated position of the origin of each of the 158 documented rockfalls are shown in Figure 4. The majority (≈ 60%) of rockfalls repeatedly originate from three primary areas (clusters) prior to the Leo slope failure and generally occur along the boundaries of the ultimate slope collapse with less than 10% originating from the centre of the Main Leo segment Figure 4. The right-most (west) cluster one appears to be coincident with the Lark Bed (a sedimentary contact reactivated as a fault), the future right-release of the Main Leo segment of the initial slope failure. Clusters 2 and 3 appear to be coincident with a location along the multiphase left-release of the Main Leo segment. Cluster 2 also appears to be positioned up-slope (within 30 m or 100 ft) of a previous one to two-bench failure. Rockfalls do not appear to originate along the farthest left-release, the Left Leo segment of the failure (tertiary failure-phase described in Section 3). Origins of rockfalls generally elucidate the ultimate head-scarp of the Main Leo failure but do not appear to define an initial break-out at the base of the slope failure.

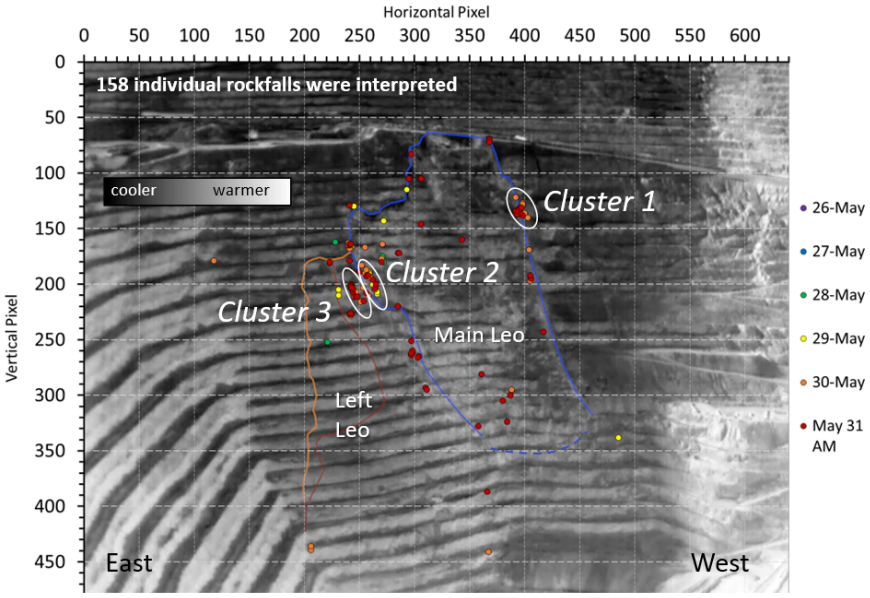

Figure 4 Still image from the thermal camera at approximately 7:30 am, 31 May with locations of rockfalls occurring from 26 to 31 May. Also shown are the future slope-failure boundaries

Plotting the cumulative total number of documented rockfalls versus time indicates that approximately 45% of the documented rockfalls occur within six hours of failure Figure 5. The day-by-day sequential occurrence of initial rockfall positions are shown in Figure 6, spanning the same pre-failure time-interval as Figure 5. Spatial clusters of rockfalls are discernible from May 27–30 and correspond to the abrupt accelerations in cumulative rockfall curve (Figure 5). In the early morning hours of May 31, rockfalls began to originate more frequently from the three clustered locations but also at new positions downslope, along the left and right

releases; up-slope along the future head-scarp; and downslope in the lower, central-portion of the Main Leo segment (Figure 6, 31 May am). Within the hour leading up to failure, the mean time between successive rockfalls is around 20 seconds, and within two minutes of failure, nearly a dozen rockfalls were documented.

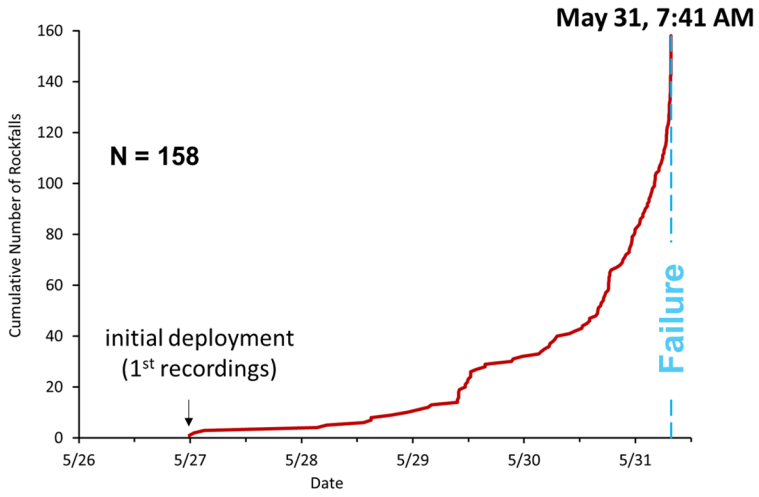

Figure 5 Plot of cumulative rockfalls versus time leading up to the Leo Failure

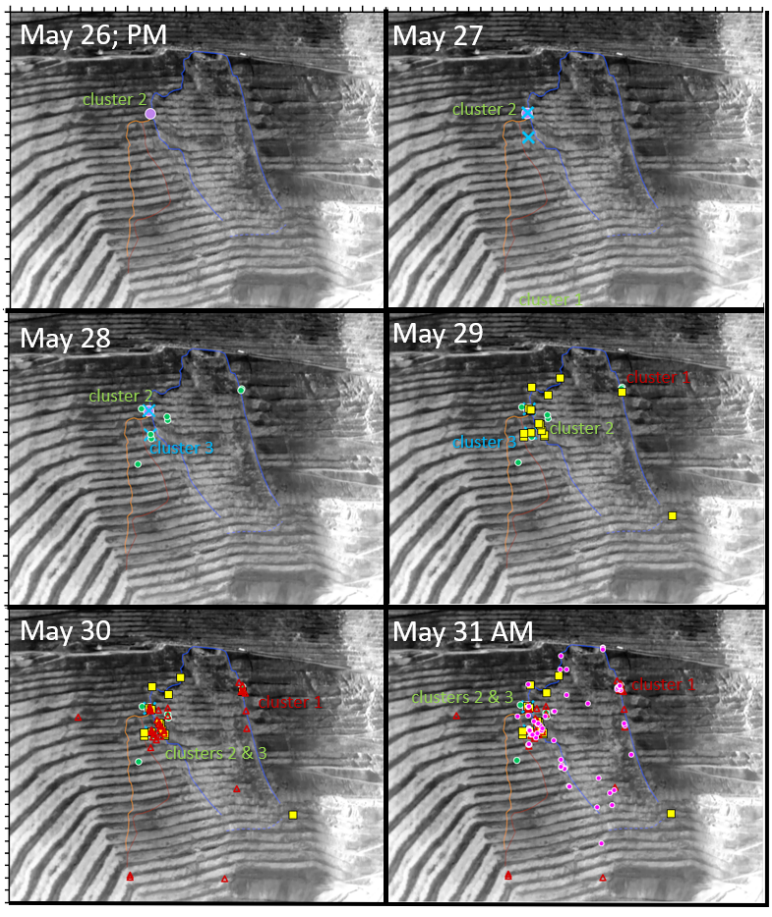

Figure 6 Still image at 7:30 am on 31 May from thermal video with day-to-day addition of positions of rockfall origins for each day leading up the Leo Failure. The image is the same for each day shown

The cumulative rockfall versus time curve exhibits cyclical behaviour similar to time-dependent, displacement curves (*sensu* Broadbent & Zavodni 1982) where abrupt increases or decreases in rockfall frequency, may be considered a proxy for progressive or regressive stage developments, respectively.

Plotting the cumulative total number of rockfalls along-side a radar-derived, displacement time-series (representing the entire Main Leo) indicates the documented rockfalls occur within the span of time characterised by the final, tertiary acceleration phase; i.e. the average of the Main Leo segment is smoothly accelerating (Figure 7). In addition, radar-displacement time-series for areas corresponding to the individual rockfall cluster areas are also smoothly accelerating, although the area of Cluster 1 exhibits a greater total displacement magnitude. Clusters 2 and 3 are positioned where there is a high, radar-derived displacement-gradient; i.e. displacement decreases abruptly laterally along-slope and across the future, failure boundaries.

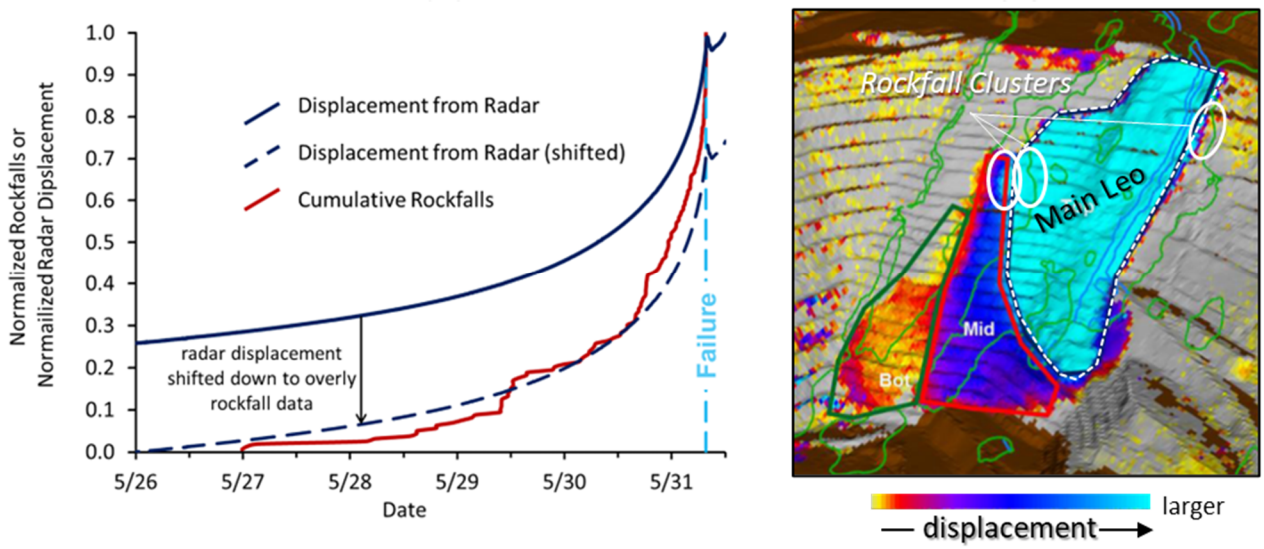

(a) (b)

Figure 7 (a) Normalised cumulative rockfalls versus time for the primary, Main Leo Failure and normalised radar-displacement data for the Main Leo segment of the failure. (b) 3D perspective view of radar-displacement data with failure boundaries and rockfall cluster locations overlain

Cumulative rockfalls versus time for the sum of the combined rockfall clusters (sum of Clusters 1, 2, 3) indicates that the cyclical behaviour of the total cumulative rockfalls is governed primarily by the behaviour of the clusters (Figure 8). Plotting the cumulative rockfalls for the individual clusters indicates that Cluster 2 is the primary influence on the cyclical behaviour of total cumulative rockfall curve (Figure 9). Cluster 3 imparts a secondary influence on the cyclical behaviour with Cluster 1 having a relatively minor influence. Approximately twice the number of rockfalls originate from each of both Cluster 2 (N = 44) and 3 (N = 33) as compared to Cluster 1 (N = 19). The first rockfall identified in the video data initiates at Cluster 2, within the final few hours of May 26. An additional rockfall initiates from Cluster 2 just an hour later on May 27. In contrast, rockfalls do not appear to initiate at Cluster 1 until approximately mid-day on May 28, 1.5 days after recording began.

Relative to Clusters 2 and 3, the cumulative rockfall versus time curve for Cluster 1, located along the contiguous faulted-bedding right-release, generally exhibits a progressive acceleration of rockfalls up to the time of failure with perhaps one relatively minor abrupt acceleration cycle occurring during the afternoon of May 30. In contrast, a cumulative rockfall curve for Cluster 2, along a geometrically complex left-release, exhibits a series of at least three abrupt cycles of rapid rockfall accelerations (e.g. 1–1.5 per day to 70–75 per day). Cluster 3 also located along the geometrically complex left-release exhibits an abrupt acceleration cycle during the morning of 30 May and series of up to five high-frequency cycles beginning in the afternoon of 30 May and continuing to approximately 05:00 hrs on 31 May before the final rockfall acceleration leading to the time of failure at 07:31 hrs (Figure 9). A plot of the first-derivative of cumulative frequency curves for each cluster demonstrates both the higher frequency and magnitude of cyclical rockfall accelerations for Clusters 2 and 3 with respect to Cluster 1 (Figure 9).

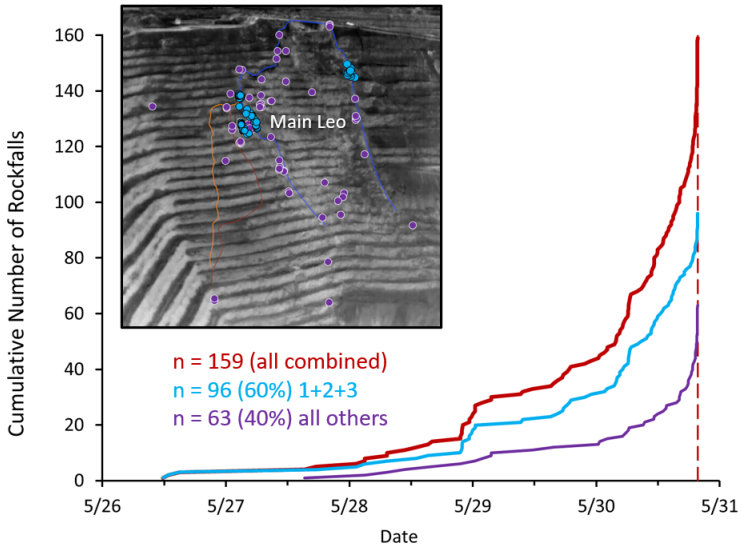

Figure 8 **Cumulative rockfalls versus time curve representing the entire population of observed rockfalls (red); the population of rockfalls originating from any of the three cluster locations; and the population of rockfalls that do not originate from any of the three clusters identified (purple). Inset is a thermal image with the positions of rockfalls belonging to a cluster (blue) and those not belonging to a cluster (purple)**

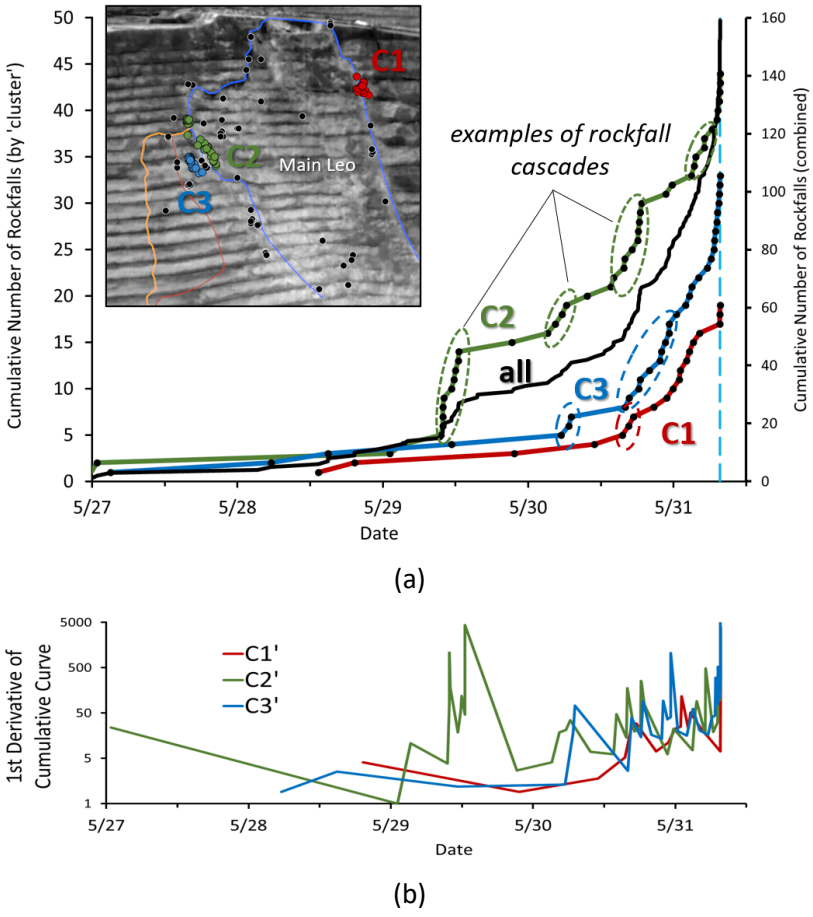

Figure 9 **(a) Cumulative rockfalls versus time curve representing the entire population of observed rockfalls (black); the population of rockfalls originating from Cluster 1 (red); Cluster 2 (green); and Cluster 3 (blue). Inset is a thermal image with the positions of rockfalls belonging to a Clusters 1-3; (b) Plot of the first-derivative for each of the three cluster curves in (a)**

5 Discussion

The Leo Failure occurred on May 31, 2021, in three stages (or modes) and in general, propagated from west to east as the mass moved downslope. The first stage of the failure (Main Leo) is bound to the west by the Lark Bed (right-release) and to the east by an intrusive igneous contact of PQM with monzonite (left-release). The Lark Bed is a relatively contiguous sedimentary, lithologic contact tectonically reactivated as a bedding-parallel fault (Figure 10). The Lark Bed is primarily a carbonate unit associated with an Upper Pennsylvanian succession of shallow-marine (upper-slope) siliciclastic and carbonate deposits. Deposition of the Lark occurred upon a low-relief seabed with no more than a few degrees of dip-variation over tens of km of depositional profile. These depositional surfaces are contiguous and often can be traced for tens up to approximately 100 km. More important, the original depositional continuity of the Lark Bed is much greater than the scale of the Leo Failure. The gouge within the core of the Lark bedding-parallel fault includes both clay-sized grains and clay minerals with relatively low strength values (see Section 3).

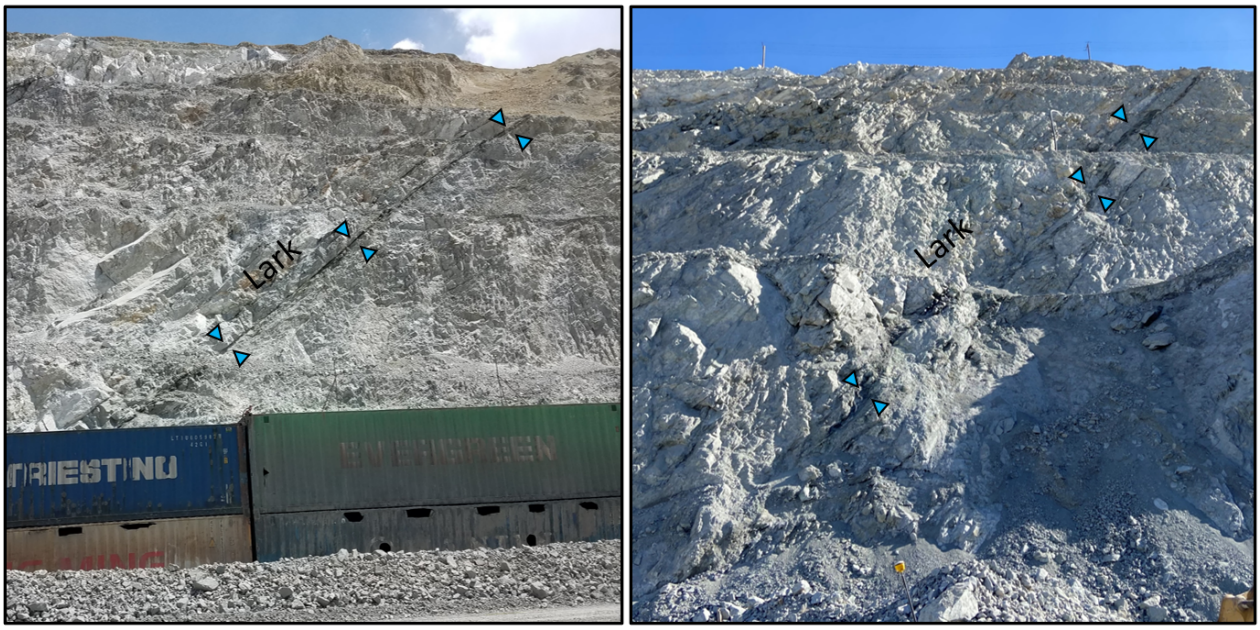

(a) (b)

Figure 10 Photographs of the Lark bed and associated bedding-parallel fault captured from (a) the 5840 bench and (b) the 5590 bench. The opposing blue triangles denote examples of where the exposed fault can be readily observed in the bench face. Each bench is approximately 15 m (50 ft) tall. The photographs document the occurrence and continuity of the fault, at a spatial scale of over 150 m, in both the strike and dip directions

In contrast to the Lark bedding-parallel fault, the left-release of the Main Leo is geometrically complex. The left-release appears to be controlled, in-part by successive igneous intrusive contacts with a variable distribution and density of structural discontinuities and spatially-varying intensity of hydrothermal alteration (Figure 11). The geometry of the intrusive contacts are relatively complex where the orientation changes tens of degrees for both strike and dip over tens of metres. Likewise, the structural fabric is also complex and characterised by ubiquitous fractures with highly diverse structural orientations ranging 60° in dip and at least 180° of dip azimuth over tens of m of slope. In contrast to the right-release, the left- and back-releases require exploitation of a geometrically complex system of structural fabric and intrusive contacts.

The cyclical accelerations of Clusters 2 and 3 and the greater number of rockfalls are interpreted to represent precursory, damage accumulation related to brittle strain localisation along sub-surface geometric asperities associated with a geometrically complex system of lithologic contacts, structural discontinuities, and variable distribution of rock mass strength. As the ‘step-path’ along the future left-release evolved, through a complex

linkage of fracture reactivation and generation, strain (displacement) is propagated to the surface such that rocks are dislodged, generating rockfalls.

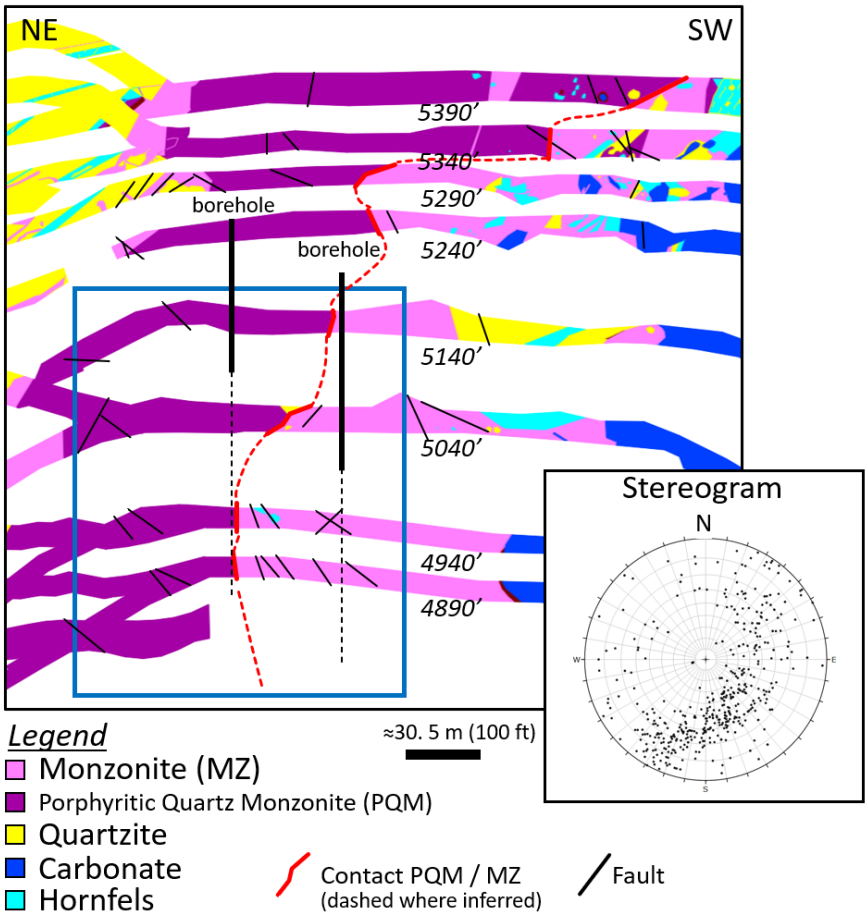

Figure 11 Pseudo geologic-section of bench-face geologic mapping in the vicinity of the structurally complex intrusive igneous contact and spatially coincident left-release of the Leo Failure. At this location, the Main Leo, left-release generally follows the contact between MZ and PQM. The elevation increases to the top of the pseudo section. The bench mapping characterises the geology over 150 m in the vertical direction and 200 m in the horizontal direction. The inset is a lower-hemisphere stereo plot of poles to all structural discontinuities identified in both the surface mapping and borehole data for both PQM and MZ rock units. The borehole traces are dashed where they descend below the section elevation. The blue rectangle indicates the area from which Rockfall Clusters 2 and 3 originate. See Figure 2 for the location of this figure

A total of approximately 32 rockfalls (20% of total) have been interpreted to have initiated along the right-release of the Main Leo. The majority of those rockfalls (N = 21) occur within approximately 6 hrs of the Leo Failure. Rockfalls along the back-release exhibit a similar spatial distribution and frequency with six of eight rockfalls occurring within approximately 6 hours of the failure.

We interpret the relatively late and relatively low number of rockfalls along the right-release to be associated with either strain softening or creep-strain along an inherited, clay-rich sedimentary contact reactivated as a quasi-planar fault (Figure 12). The faulted sedimentary contact is weak and relatively smooth and strain accommodation could occur without the need to localise significant brittle strain and accumulate damage such that rockfalls occur. Cluster 1, the exception, overlies the sole portion of the failure slide-surface that exhibits geometric irregularity. In addition, the cumulative rockfalls versus time curve exhibits a relatively smooth acceleration and lacks abrupt cyclic accelerations when compared to the cumulative rockfall curves

for Clusters 2 and 3. Cluster 1 could be associated with a relatively minor geometric asperity along the right-release, Lark bedding-parallel fault.

We have inferred that a strain softening or creep-strain constitutive behaviour governs pre-collapse, displacement along the Lark bedding-parallel fault and that a pressure-dependent, constitutive behaviour, e.g. fracture (or lithologic contact) reactivation and/or fracture generation governs the complex left-release. This is consistent with a high strain gradient (e.g. displacement) that abruptly decreases laterally across the location of the left-release and Clusters 2 and 3. Differential lateral strain coupled with both the observed late occurrences and paucity of rockfalls along the back-release, implies that both the right- and left-release could have been active earlier and collapse occurred through a final step-path linkage to form the back-release.

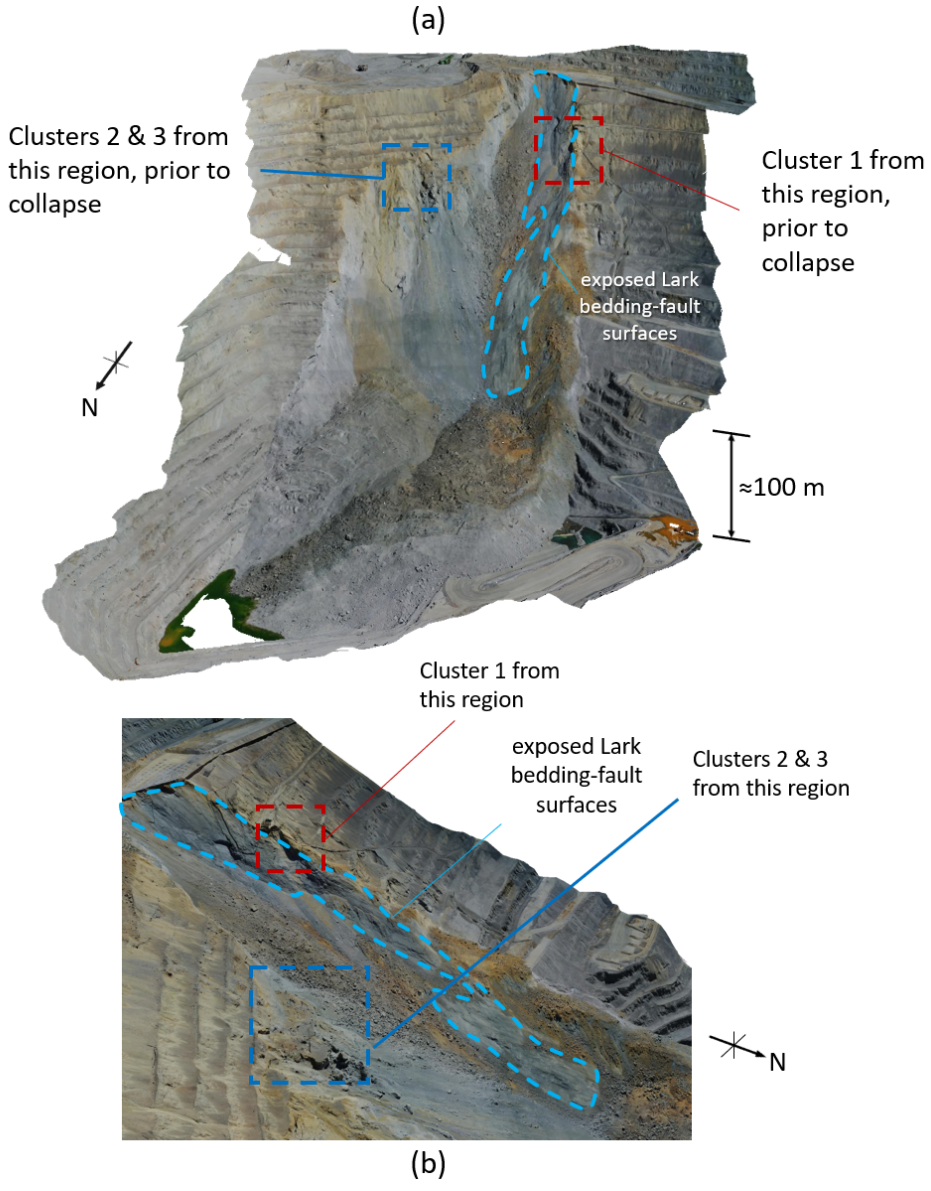

Figure 12 3D perspective views of the Leo Failure captured from aerial 3D photogrammetry collected in the hours following collapse. (a) View of the failure with locations of identified rockfall clusters. (b) View from the east (left side) of the Lark bedding-parallel fault, sliding surfaces. Note the pervasive striations developed and exposed on the quasi-planar sliding surface

6 Conclusion

Based upon continuous thermal video recordings we document the occurrence of rockfalls leading to a large (19×10^6 tonnes) slope failure (Leo Failure) at the Bingham Canyon Mine, Utah, USA. The frequency of rockfalls increases exponentially leading to failure, with approximately 45% of the total documented rockfalls (158) occurring within 6 hours of the failure. The exponential or power-law acceleration in rockfalls represent precursory plastic-strain (or, damage accumulation) indicators of the slope collapse. Although precursory rockfalls have been documented for natural slopes, this is the first known documentation of precursory rockfalls leading to an open pit mine slope collapse. The majority (88%) of rockfalls originate along the right, a left-, and the back-release, but not the break-out at the toe. The majority of rockfalls (60%) repeatedly originate from nearly the same positions within three different areas (clusters): Cluster 1 positioned along the right-release, a bedding-parallel fault with clay-gouge; and both Clusters 2 and 3 positioned along a multi-staged left-release, a complex intra-intrusive, faulted igneous contact. Approximately twice the number of rockfalls originate from each of both Cluster 2 (N = 44) and 3 (N = 33) as compared to Cluster 1 (N = 19). The cumulative rockfall versus time curve for Cluster 1, along the contiguous faulted-bedding right-release, generally exhibits a progressive acceleration up to the time of failure. In contrast, a cumulative rockfall curve for cluster 2, along a geometrically complex left-release, exhibits a series of three abrupt periods of rapid rockfall accelerations (rockfall 'cascades' or 'swarms'). The cyclical accelerations and greater number of rockfalls are attributed to brittle strain localisation at geometric asperities associated with an evolving 'step-path' left-release, as opposed to creep-strain along an inherited, clay-rich sedimentary contact reactivated as a fault.

References

Armitrano, D. Grasso, JR & Senfaute, G 2005, 'Seismic precursory patterns before a cliff collapse and critical point phenomena', *Geophysical Research Letters*, vol. 32.

Broadbent, C & Zavodni, Z 1982, 'Influence of rock structures on stability, in stability in surface mining', *Society of Mining Engineers*, vol. 3.

Byerlee, J 1978, 'A review of rock mechanics studies in the United States pertinent to earthquake prediction', *PAGEOPH*, vol. 116, https://doi.org/10.1007/BF00876526

Fukuzonu, T 1985, 'Inverse velocity over time a new method for predicting the failure time of a slope', *Proceedings of the IVth International Conference and Field Workshop on Landslides*.

Hobbs, BE 1976, *An Outline of Structural Geology*, John Wiley & Sons, Hoboken.

Kemeny, J 1991, 'A model for non-linear rock deformation under compression due to sub-critical crack growth', *International Journal of Rock Mechanics and Mining Sciences*, vol. 28, no. 6, pp. 459–467.

Kromer, R, Hutchison, J, Lato, M & Gauthier, D 2015, 'Identifying rock slope failure precursors using LiDAR for transportation corridor hazard management', *Engineering Geology* , vol. 195.

Lockner, D & Byerlee, J 1992, 'Fault growth and acoustic emissions in confined granite', *American Society of Mechanical Engineers Applied Mechanical Reviews*, vol. 45, no. 3.

Lockner, D 1993, 'Room temperature creep in saturated granite', *Journal of Geophysical Research: Solid Earth* , vol. 98, no. B1, pp. 475–487.

Read, J & Stacey, P 2009, *Guidelines for Open Pit Slope Design*, CSIRO Publishing, Melbourne.

Rose, ND & Hungr, O 2006, 'Forecasting potential slope failure in open pit mines – contingency planning and remediation', *International Journal of Rock Mechanics and Mining Sciences*, vol. 44.

Rosser, N, Lim, M, Petley, D, Dunning, S & Allison, R 2007, 'Patterns of precursory rockfall prior to slope failure', *Journal of Geophysical Research*, vol. 112, F04014, https://doi.org/10.1029/2006jf000642

Shao, J, Duveau, G, Hoteit, N, Sibai, M. & Bart, M. 1997, 'Time Dependent Continuous Damage Model for Deformation and Failure of Brittle Rock', *International Journal of Rock Mechanics and Mining Sciences*, vol. 34, no. 3-4.

Senfaute, G, Duperret, A & Lawrence, J 2009, 'Micro-seismic precursory cracks prior to rock-fall on coastal chalk cliffs: a case study at Mesnil-Val, Normandie, NW France', *Natural Hazards and Earth System Sciences*, vol. 9, pp. 1625–1641.

Voight, BA 1988, 'A method for prediction of volcanic eruptions', *Nature*, no. 332, pp. 125–130.

Wellman, E, Schafer, K, Williams, C & Ross, B 2022, 'Thermal imaging for rockfall detection', paper presented at 56th U.S. Rock Mechanics/Geomechanics Symposium, Santa Fe, https://doi.org/10.56952/ARMA-2022-0430

Zavodni, Z 2001, 'Time-dependent movements of open-pit slopes', *SME Proceedings*, Society for Mining, Metallurgy & Exploration, Englewood, pp. 81–87.